An X-Ray-dim "Isolated" Neutron Star in a Binary?

Jie Lin[1,2,3] , Chunqian Li[4,5] , Weiyang Wang[1,2,3] , Heng Xu[6] , Jinchen Jiang[6] , Daoye Yang[4], Shahidin Yaqup[7],
Abdusamatjan Iskanda[7], Shuguo Ma[7] , Hubiao Niu[7] , Ali Esamdin[7] , Shuai Liu[4], Gavin Ramsay[8] , Jose I. Vines[9],
Jianrong Shi[4,5] , and Renxin Xu[1,2,3]

[1] Department of Astronomy, Peking University, Beijing 100871, People's Republic of China; r.x.xu@pku.edu.cn
[2] State Key Laboratory of Nuclear Physics and Technology, School of Physics, Peking University, Beijing 100871, People's Republic of China
[3] Kavli Institute for Astronomy and Astrophysics, Peking University, Beijing 100871, People's Republic of China
[4] CAS Key Laboratory of Optical Astronomy, National Astronomical Observatories, Chinese Academy of Sciences, Beijing 100101, People's Republic of China
sjr@nao.cas.cn
[5] School of Astronomy and Space Science, University of Chinese Academy of Sciences, Beijing 100049, People's Republic of China
[6] National Astronomical Observatories, Chinese Academy of Sciences, Beijing 100101, People's Republic of China
[7] XinJiang Astronomical Observatory, Chinese Academy of Sciences, People's Republic of China
[8] Armagh Observatory and Planetarium, College Hill, Armagh BT61 9DG, UK
[9] Departamento de Astronomía, Universidad de Chile, Casilla 36-D, Santiago, Chile
Received 2022 October 14; revised 2023 January 18; accepted 2023 January 22; published 2023 February 9

Abstract

We report the discovery of a dark companion to 2MASS J15274848+3536572 with an orbital period of 6.14 hr. Combining the radial velocity from LAMOST observations and modeling of the multiband light curve, one obtains a mass function of $\simeq 0.131\,M_\odot$, an inclination of $45°.20^{+0°.13}_{-0°.20}$, and a mass ratio of $0.631^{+0.014}_{-0.003}$, which demonstrate the binary nature of the dark companion with a mass of $0.98 \pm 0.03\,M_\odot$ and a main-sequence K9–M0 star of $0.62 \pm 0.01\,M_\odot$. LAMOST optical spectra at a range of orbital phases reveal extra-peaked H_α emission that suggests the presence of an accretion disk. The dark companion does not seem to be a white dwarf because of the lack of any observed dwarf nova outbursts in the long-term data archive, although a magnetic white dwarf cannot be excluded. Alternatively, we propose a scenario wherein the dark companion is a neutron star, but we have not detected radio pulsations or a single pulse from the system with the FAST (Five-hundred-meter Aperture Spherical radio Telescope), which hints at a radio-quiet compact object. If the dark companion is identified as a neutron star, it will be the nearest (∼118 pc) and lightest neutron star. Furthermore, kinematic analysis of the system's orbit in the galaxy may suggest its supernova event is associated with the radionuclide ^{60}Fe signal observed from deep-sea crusts. This radio-quiet and X-ray-dim nearby neutron star may resemble an XDINS (X-ray-dim isolated neutron star) but in a binary.

Unified Astronomy Thesaurus concepts: Cataclysmic variable stars (203); Neutron stars (1108)

1. Introduction

The puzzling equation of the state of dense matter inside neutron stars (NSs) is focused on both microphysics and astrophysics, and moreover, the diversity of NS manifestations challenges a simple belief about their astronomical origins (e.g., Kaspi 2010). Among the populations in the NS zoo, there is a small group called X-ray-dim isolated NSs (XDINSs), characterized by low thermal X-ray luminosity within a few hundreds of parsecs. Is there any XDINS-like compact object in a binary? How can one find it? This is the focus of the present work.

Up to now, only seven XDINSs have been discovered by the ROSAT all-sky observations, nicknamed the Magnificent Seven (Voges et al. 1996). They have an intriguing feature; that is, they are characterized by Planck-like spectra in X-ray bands as well as in optical bands but with an ordered excess, and by the nondetection of radio signals (Haberl 2007). XDINSs are peculiar objects for revealing the equation of state (EOS) at supranuclear density and offer an unprecedented opportunity to study atmospheric emission on the surface (e.g., Ho et al. 2007; Wang et al. 2017, 2018). If similar objects can

be discovered outside our local volume, it will be significant for understanding their properties as a group and their relationship to other galactic isolated NS (INS) families. A promising INS candidate was found from the 2XMMp catalog of serendipitous sources (Pires et al. 2009), and four newly discovered INS (isolated NS) candidates were reported from the 4XMM-DR10 catalog (Rigoselli et al. 2022). Such stars are measured to be close to us (∼120–500 pc), and as numerous as young radio and γ-ray pulsars locally, suggesting that there may be lots of similar Galactic sources still unknown.

We focus on binary systems with compact objects, which can provide an opportunity to develop the accretion disk model and test the prediction of binary interaction theories (Langer 2012; Mukai 2017). Interestingly, NSs with XDINS-like characteristics, which are of great interest in the EOS problem, have not been found in binaries yet (e.g., Pires et al. 2015). In addition, the discovery and observed mass distributions of NSs and black holes (BHs) in the Milky Way are crucial for understanding core-collapse supernovae and the evolution of massive stars (Fryer et al. 2012; Woosley et al. 2020). So far, most compact binaries with NSs or BHs are identified from radio, X-ray, and gamma-ray surveys and from gravitational waves. However, these compact binaries identified based on the above methods may represent only a small fraction of the overall population of compact objects, resulting from accreting at a sufficiently low rate or in long quiescent periods. Here,
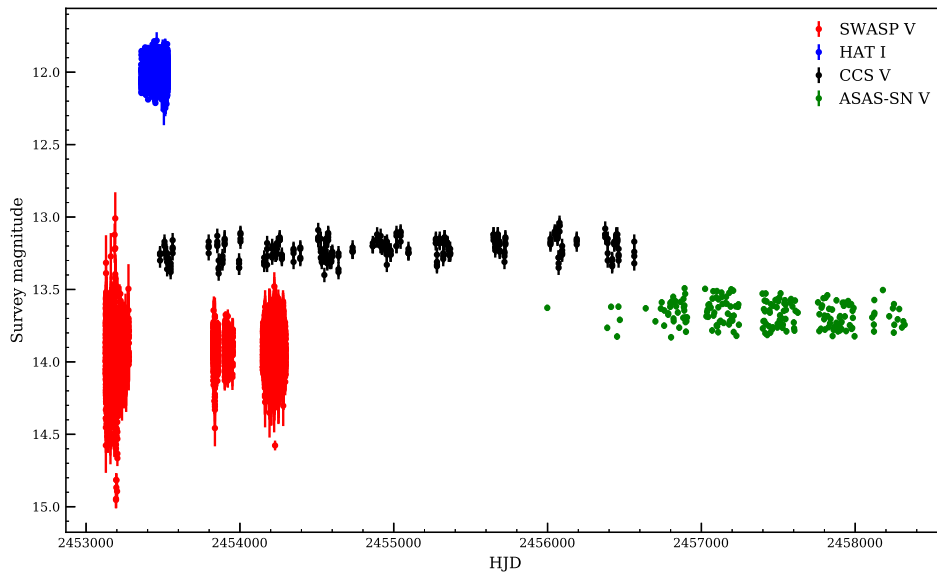
Figure 1. SuperWASP, HATNet, CCS, and ASAS-SN photometry for J1527 from 2004 May 2 to 2018 July 22. No evidence for outbursts appears in the total 5193 day time span.

radial-velocity modulation in optical spectra is a promising method to uncover unseen compact objects that have a stellar companion (Gu et al. 2019; Liu et al. 2019; Thompson et al. 2019; Yuan et al. 2022). More recently, a nonaccreting NS candidate was discovered by synergizing optical time-domain spectroscopy (Yi et al. 2022).

Here we present the first optical spectroscopy and multiband optical photometry of a single-line binary, 2MASS J15274848 +3536572 (hereafter J1527), and report that it consists of a K9-M0 main-sequence and unseen companion of $M_c = 0.98 \pm 0.03$ $M_\odot$. We also discuss two possible scenarios wherein the dark companion of J1527 is a white dwarf or NS candidate, respectively. This paper is organized as follows. We describe observations of the source in Section 2 and analyze these observations to extract the physical parameters of the source in Section 3. A general discussion of the dark companion is in Section 4. Our conclusions are presented in Section 5.

2. Observations

2.1. Optical Photometry and Open-source Data

J1527 was also observed with the Nanshan 1 m Wide-field Telescope (NOWT) (Bai et al. 2020) of Xinjiang Astronomical Observatory from 2022 April 15 to 17 for three nights in the B, V, and R bands. The exposure time for each filter is 30 s, and the total observation time of each run in the B, V, and R bands is about 220 s. All the raw images for the three bands were overscan-corrected, bias-subtracted, and flat-fielded using IRAF (Tody 1986, 1993). The optimized aperture photometry was employed using the software Sextractor (Bertin & Arnouts 1996). The resulting differential photometry is relative to a nearby stable reference star in the field, which is insensitive to thin clouds or moderate atmospheric variability.

J1527 was classified as a contact eclipsing binary in the All-Sky Automated Survey (ASAS) and the Catalina Sky surveys (CSS) with a period of $P = 0.2556686$ days (Drake et al. 2014; Jayasinghe et al. 2019). We obtained sampled light curves from ASAS and CSS and a densely sampled light curve from the SuperWASP with ∼300 s cadence and the Transiting Exoplanet Survey Telescope (TESS) and Hungarian Automated Telescope with ∼300 s cadence (HAT) (Hartman et al. 2011), which is shown in Figure 1. TIC 16320250[10] was observed by TESS in Sector 24 from 2020 April 16 to 2020 May 12. TIC 16320250 was observed with 30 minute cadence.

In addition, it also was observed with GALEX as part of the Medium Imaging Survey with measured fluxes of $(2.42 \pm 0.34) \times 10^{-13}$ and $(1.25 \pm 0.05) \times 10^{-12}$ erg cm^{-2} s^{-1} in the far- and near-ultraviolet (FUV and NUV), respectively. In Gaia EDR3, the source_id of J1527 is 1375051479376039040 (Gaia Collaboration et al. 2021). Its EDR3 parallax of $\omega_{EDR3} = 8.44844 \pm 0.011068$ mas implies a distance of $d = 118.13 \pm 0.86$ pc, which is consistent with its Gaia DR2 parallax. Gaia DR2 also reports a luminosity $L_{Gaia} = 0.101161 \pm 0.000605 \, L_\odot$, temperature $T_{eff,Gaia} = 4047^{+171}_{-109}$ K, and radius $R_{Gaia} = 0.65^{+0.03}_{-0.05} \, R_\odot$ for the star (Gaia Collaboration et al. 2018).

2.2. Optical Spectra

The Large Sky Area Multi-Object fiber Spectroscopic Telescope (LAMOST) is a 4 m Schmidt telescope with a 5° field of view and has become the first spectroscopic survey to collect tens of millions of spectra from the universe with both medium-resolution and low-resolution modes. The medium-resolution observations have $R \sim 7500$ with both blue and red arms at a limiting magnitude $G = 15$ mag (Zong et al. 2020). The wavelength coverage of the blue arm is from 495 to 535 nm, while it is from 630 to 680 nm for the red arm. The low-resolution observation mode has a limiting magnitude as faint as $r \sim 17.8$ mag. with a resolution of $R \sim 1800$, and the wavelength range is from 370 to 900 nm (Zhao et al. 2012).

Here, we obtained 2 low-resolution spectra and 10 medium-resolution spectra of J1527 from the LAMOST archive data. The low-resolution LAMOST spectra indicate it to be a K9-M0 type star (Figure 2) with clear signs of the Ca II H&K and Balmer H$_\alpha$ and H$_\beta$ emission lines, which tell us it has chromospheric activity. However, the H$_\alpha$ emission shows a wider range and a complex morphology including an extra

---

[10] The data are available at the Mikulski Archive for Space Telescopes (MAST) at the Space Telescope Science Institute: doi:10.17909/e21w-k824.
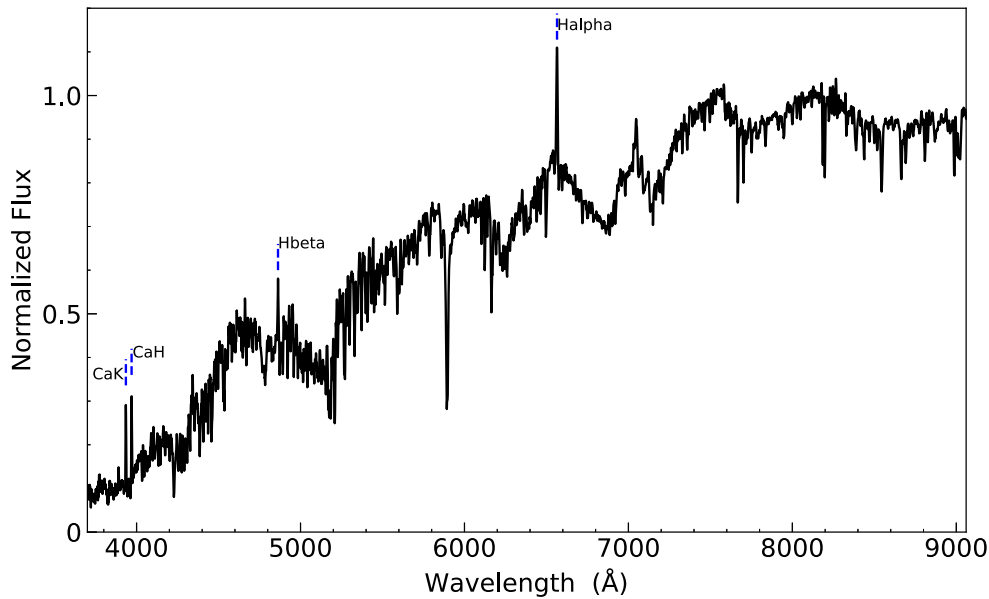
Figure 2. Low-resolution LAMOST spectrum from 2020 January 22, showing the K9-M0 spectral type star and the clear Ca II H&K and Balmer H_α and H_β emission lines.

peak emission profile in many observations, which may suggest the presence of an accretion disk. We derived the barycentric velocity of each spectrum through the cross-correlation technique. Here, the emission lines of two low-resolution spectra have been excised in the cross-correlation process. For the 10 medium-resolution spectra, only the spectra of the blue arms have been chosen to measure radial velocities due to the lack of emission lines in the blue range. The cross-correlation was performed using the spectral template ($T_{eff} = 4500$ K, log $g = 4.5$, [Fe/H] $= -1.0$) calculated with the Kurucz model (Castelli & Kurucz 2003).

In addition, we estimate the projected rotational velocity $v \sin i$ using the red arms of the medium-resolution LAMOST spectra because of its high signal-to-noise ratio. A $\mathcal{X}^2$ minimization was performed to constrain the projected rotational velocity $v \sin i$ using the above spectral template with a range of $v \sin i$ from 0 to 300 km s^{-1}. The mean value obtained from the six medium-resolution LAMOST spectra is $v \sin i = 94 \pm 5$ km s^{-1}. The quoted uncertainty in this value is the standard deviation. Furthermore, high-resolution spectra will confirm and improve this measurement in the future.

2.3. Radio and X-Ray Observations

We searched for radio pulsations using FAST (Five-hundred-meter Aperture Spherical radio Telescope). The central frequency and bandwidth of the receiver of FAST are 1250 and 400 MHz, respectively (Jiang et al. 2020). Observations were acquired using the central beam of the 19 beam receiver, which is 25 K for the system temperature. J1527 was observed for 40 minutes and 50 minutes on 2021 October 28 and 2022 September 14, respectively. Using the PRESTO pulsar search suite (Ransom 2001), we excised radio frequency interference and performed an acceleration search to retain sensitivity by setting the zmax value to 200, as well as trial dispersion measures between 0 and 22 pc cm^{-3}. In addition, 1RXS J152748.8+353658 was listed in the ROSAT ALL-Sky Survey Source Catalogue as a faint X-ray source (Voges et al. 1999), with a count rate of 0.0316 cts s^{-1} in the 0.1–2.4 keV PSPC range. More recently, the RASS was

reprocessed by Boller et al. (2016). The count rate (count rate 0.0342 ± 0.0122 cts s^{-1}) and the hardness ratio (HR1[11] $= 0.77 \pm 0.27$; HR2 $= -0.66 \pm 0.19$) were updated, which indicate a relatively soft emission spectrum. The observed flux is $5.54 \pm 2.98 \times 10^{-14}$ erg cm^{-2} s^{-1} (0.1–2.4 keV) using the energy to count conversion factor (ECF $= 1.62 \times 10^{-12}$ erg cm^{-2} s^{-1} counts^{-1}) adopting a black-body model with a temperature of $\sim$95.6 eV and a column density of $\sim 0.41 \times 10^{20}$ cm^{-2} as in Haberl et al. (2004).

3. Results

3.1. Properties of the Main-sequence K9-M0 Star

We obtained the surface temperatures (T_{eff}) and radius (R) of the K9-M0 type star by fitting the spectral energy distribution (SED) using astroARIADNE (Vines & Jenkins 2022). For the SED, we used the photometry from Gaia DR3 (G, G_{BP}, and G_{RP}), 2MASS (J, H, and K_s), SDSS (u, g, r, i, and z), Pan-STARRS (g and y), JOHNSON (B and V), WISE (W1 and W2) and TESS (T). We found an excellent fit by using the extinction parameters $A_v = 0$ derived from three-dimensional dust maps of Green et al. (2019), with $T_{eff} = 3896.42^{+32.70}_{-46.12}$ K and $R = 0.689^{+0.020}_{-0.012} R_\odot$ (Figure 3), which are consistent with that of Gaia DR2. However, the parameter extinction (0.38) from DR2 in the G band is different from that in the three-dimensional dust maps of Green et al. (2019). This may result from Green et al. (2019) leveraging a greater number of photometric passbands compared to two independent passbands for Gaia DR2 and delivering typical reddening uncertainties that are lower. In addition, the SED fit yields $T_{eff} = 3919.02^{+30.55}_{-39.58}$ K, $R = 0.685^{+0.016}_{-0.010} R_\odot$, and $A_v = 0.03^{+0.01}_{-0.02}$ using the free extinction parameters. The results of the SED fit suggest the spectral type of the main-sequence star is K9-M0 and demonstrate the presence of a UV excess in the two GALEX measurements.

Figure 4 shows the variations of the H_α emission-line profiles with orbital phase, which are corrected to the rest frame

---

[11] The definitions of HR1 and HR2 are shown in Appendix A of Boller et al. (2016).
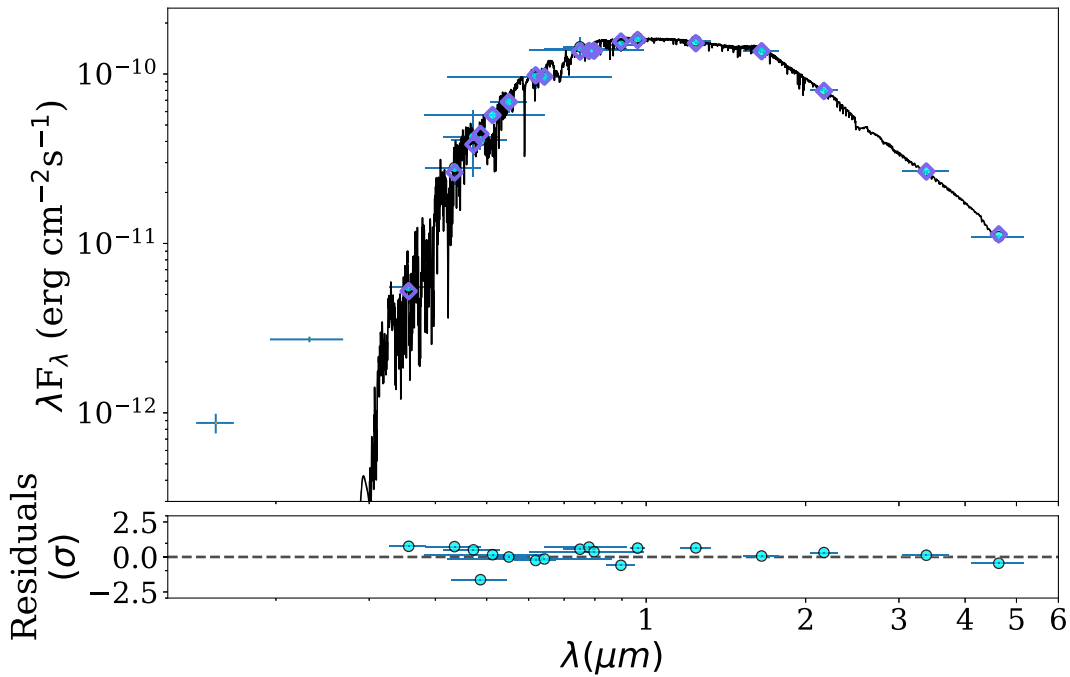
Figure 3. The best-fitting SED model for J1527 after fixing the extinction parameters $A_v = 0$. The black curve is the best-fitting model. The green pluses and circles are the retrieved photometric measures. The blue diamonds are synthetic photometry. Here, the GALEX FUV and NUV (two green pluses) were not included in the SED fitting.

of the K9-M0 star and companion, respectively. We found that the H_α profiles almost peak directly at or very near the velocity of the K9-M0 star (left panel in Figure 4). This suggests that the H_α emission results from the visible star's surface. The H_α emission tracks the orbital motion in the rest frame of the K9-M0 type star. In addition, we see the Ca II H&K emission in the low-resolution spectra, which suggested that the H_α emission could be from chromospheric activity as discussed in Section 2.2. The typical FWHM of the H_α and H_β emission profile is ~ 290 km s^{-1} in most cases, which may suggest H_β also results from chromospheric activity.

In addition, the H_α emission profile occasionally shows a broad and narrow morphology at specific phases ($\phi = 0.194; 0.743; 0.805$). Here, we transfer the H_α emission to the rest frame of the unseen object using the binary mass ratio, systemic velocity, and radial velocity of the K9-M0-type star (Right in Figure 4). We find that the peak of the narrow H_α component is almost in phase with the unseen companion at specific phases. Furthermore, in order to confirm whether the narrow component is from an accretion disk, we measure equivalent widths (EW) and radial velocities for a narrow and broad H_α at specific phases, respectively. The median EW of the narrow component (FWHM ~ 125 km s^{-1}) and broad component (FWHM ~ 250 km s^{-1}) is EW($H_{\alpha,N} = 0.53 \pm 0.13$) and EW($H_{\alpha,B} = 2.33 \pm 0.14$), respectively. We find that the narrow component is indeed in antiphase with the radial-velocity curve of the visible star (see Figure 5), while the broad component is in phase with the absorption-line radial-velocity curve. Although the presence of a broad, double-peaked H_α emission profile has generally been accepted as evidence for an accretion disk in the system (Wang et al. 2009; Strader et al. 2015), the shape of the H_α emission lines from an accretion disk depends on an inclination angle and the choice of power-law n and disk base density ρ_0 (Silaj et al. 2010). Furthermore, the narrow H_α component from an accretion disk may imply a small accretion disk around the compact object and/or a level of accretion disk activity.

One reasonable explanation for complex H_α emission may arise from a combination of an accretion disk around the dark companion and the stellar chromosphere. Here, the narrow extra-peaked H_α emission profile from an accretion disk is hard to identify when the chromosphere of the star is the main contributor to the emission. However, we also note that the H_α component from an accretion disk generally has an FWHM of the order of several hundreds to a thousand km s^{-1}. Overall, we interpret the structured peak of the H_α emission as evidence of an accretion disk, with a complicated phenomenology that deserves further study. The high-resolution and adequate phase-coverage spectroscopic observations will help us to uncover their true origin.

3.2. Radial-velocity Curves

After correcting the observation epochs to the Heliocentric Julian Date (HJD), we performed a circular Keplerian model fit to our radial-velocity data using the custom Markov Chain Monte Carlo (MCMC) sampler TheJoker (Price-Whelan et al. 2017). Here, we fit the four free parameters for the period P, the time of ascending node T_0, systemic velocity γ, and the semi-amplitude K. We obtain $P = 0.2556698 \pm 0.0000002$ days, $T_0 = 2457091.607 \pm 0.001$ days, $K = 171.09^{+1.00}_{-0.97}$ km s^{-1}, and $\gamma = -31.89^{+0.82}_{-0.80}$ km s^{-1}. We find that the spectroscopic period is basically consistent with the photometric period reported by the ASAS and CSS. The phased radial-velocity curve is shown in Figure 5. We used the posterior samples from this fit to derive the mass function $f(M)$,

$$f(M) = \frac{PK^3}{2\pi G} = \frac{M_p^3 \sin^3 i}{1+q} \qquad (1)$$

for mass ratio $q = M_p/M_c$ and inclination i. Here, we define the visible main-sequence star as the primary M_p, while M_c is the dark companion. We find $f(M) = 0.131 \pm 0.002 M_\odot$. Using the
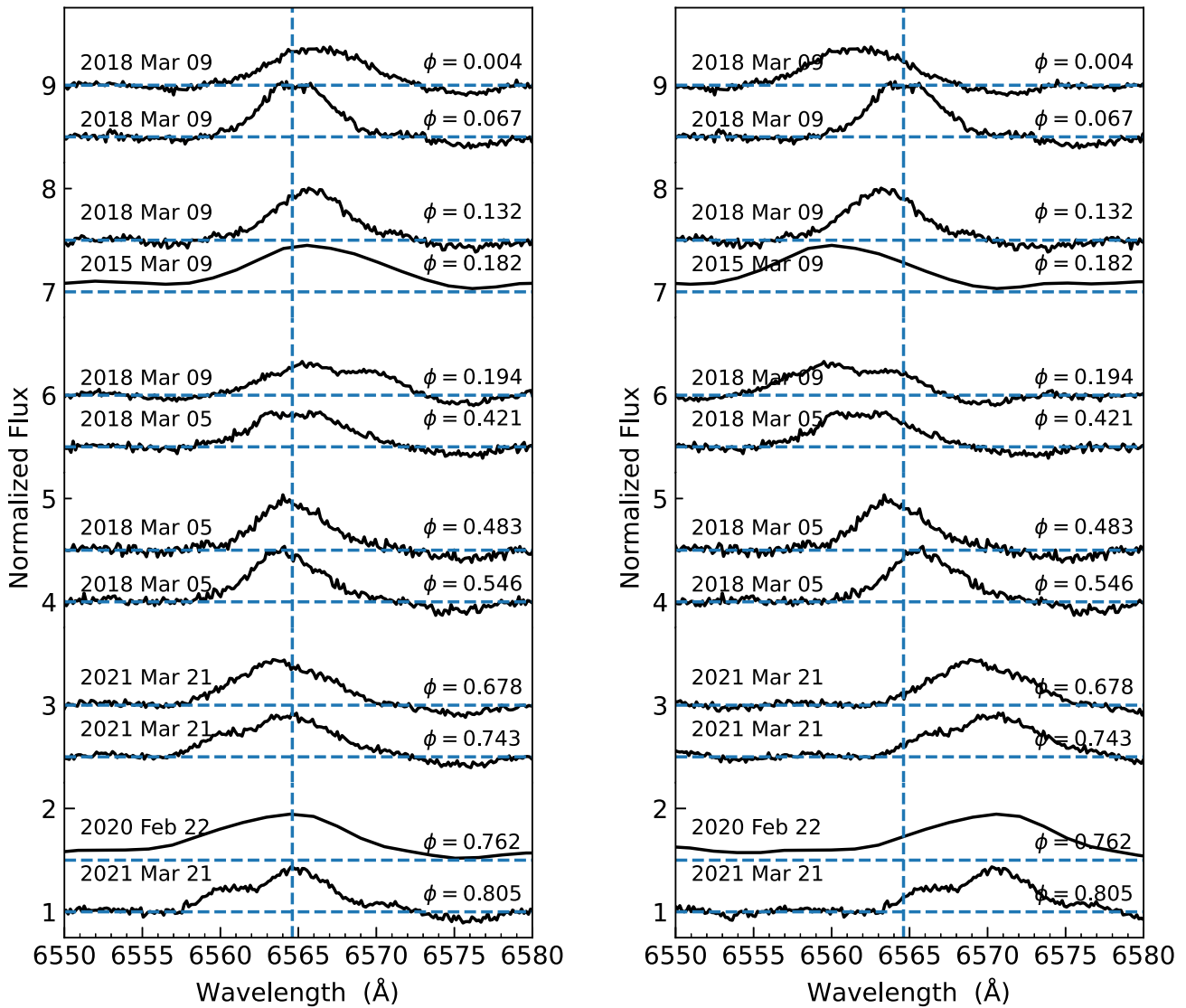
Figure 4. Left: H_{α} emission-line profiles as a function of orbital phase in the rest frame of the K9-M0 type star. Right: H_{α} emission-line profiles in the rest frame of the compact object.

measured rotational velocity and semiamplitude K, the mass ratio is $q = 0.63 \pm 0.06$ given by the standard equation $v \sin i = 0.462 K q^{1/3} (1 + q)^{2/3}$ (Casares 2001).

3.3. Light-curve Modeling

The light curves of J1527 clearly show a significant ellipsoidal variability with a rather small amplitude. The light curves are asymmetric in the phased light curve of the TESS T band, showing the fluxes of the two maxima are different, while there are two maxima and one minimum in the phased light curve of the B, V, and R bands. This suggests that the starspot patterns evolve with time as the chromospheric activity changes. Here, we assume that the visible star filling its Roche lobe, given the evidence for an accretion disk, and the accretion disk do not contribute significantly to the optical luminosity of the system due to the low X-ray luminosity of the system. Indeed, there is also no evidence of irradiation in the light curve.

To fit the B-, V-, and R-band light curves, we had to add one spot on the K9-M0 star surface with the longitude, latitude,

angular radius, and temperature factor as their parameters while two spots are needed for the TESS T band. We fit the B-, V-, and R-band light curves and independently fit the TESS T band using PHOEBE 2.4 (Conroy et al. 2020). For the dark companion, we used the option "distortion method = none" and assume a small ($R = 3 \times 10^{-6} R_{\odot}$), cold ($T_{eff} = 300$ K) blackbody, as done in Jayasinghe et al. (2021). We set the gravity darkening coefficient as $\beta = 0.32$ and limb-darkening coefficients as $(x, y) = (0.5, 0.5)$. We do not include the effects of irradiation. We initially performed trial fits to the B-, V-, and R-band light curves using Nelder–Mead simplex optimization routine. Then, the parameters from the trial fit performed an MCMC run (nwalkers = 48, niters = 1000, burnin = 150) using the emcee (Foreman-Mackey et al. 2019) solver in PHOEBE 2.4. We fit over the following parameters: the binary mass ratio $q = M_p/M_c$, orbital inclination (i), the effective temperature (T_{eff}), and one spot of the main-sequence K9-M0 star in which the parameters of the starspot include the longitude, latitude, angular radius, and temperature factor.[12]

---

[12] The ratio of the temperature of the spot to the local intrinsic value.
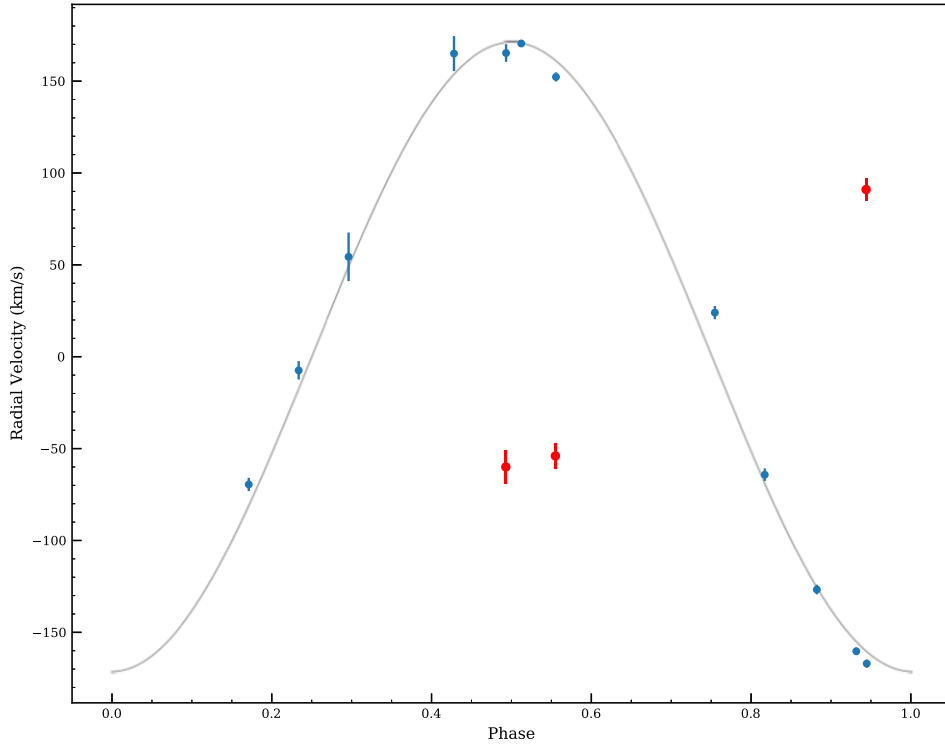
Figure 5. The observed radial velocities for J1527 as a function of the orbital phase obtained in 12 epochs from LAMOST, with the radial-velocity fit, plotted. The red velocity points are the radial velocities of the narrow H$_\alpha$ emission, which is in antiphase with the absorption-line velocities.

The results of the fitting are shown in Table 4. We also independently fit the TESS T-band light curve using two star spots and fixed the parameters of q, i, a, and $T_{\mathrm{eff,K}}$ derived from the previous fitting results. The B-, V-, R-, and T-band light curves with the best-fitting model from PHOEBE are shown in Figure 6, while the residuals of the model are shown in Figure 8 (see Appendix A). The effective temperature and Roche lobe radius ($0.67 \pm 0.01 R_\odot$) of the system derived from the PHOEBE model basically agree well with those obtained from the SED. Combining the modeling of the radial velocity and the PHOEBE model for the ellipsoidal variations, we have enough information to directly determine the masses of the two components in the system. The companion mass is

$$M_{\mathrm{c}} = \frac{f(M)(1+q)^2}{\sin^3 i} \qquad (2)$$

and from the PHOEBE models, we find that the K9–M0 main-sequence star has a mass $M_{\mathrm{p}} = 0.62 \pm 0.01\,M_\odot$ and the companion mass is $M_{\mathrm{c}} = 0.98 \pm 0.03\,M_\odot$. Based on the mass–luminosity relations from Mann et al. (2019), we obtained that the visible star has a mass of $0.63 \pm 0.02 M_\odot$, which is consistent with the one from the PHOEBE models. For the Roche lobe filling factor <1, we obtained a K9–M0 main-sequence star of $M_{\mathrm{p}} = 0.52 \pm 0.06\,M_\odot$ and an unseen companion of $M_{\mathrm{c}} = 0.87 \pm 0.10\,M_\odot$. Here, the orbital inclination and mass ratio $46°\!.65^{+0°.59}_{-0°.68}$ and $0.596^{+0.041}_{-0.065}$, respectively. However, the obtained mass and radius ($0.620^{+0.014}_{-0.035} R_\odot$) of the visible star are small than those resulting from the mass–luminosity relations and SED, which may suggest that the visible star is filling its Roche lobe (Table 1).

Table 1
The Best-fitting Parameter for the B, V, R Bands and T Band in Filling the Visible Roche Lobe, Respectively

Parameter	B, V, and R Band	T Band
P_{orb} (days)	0.2556698 (fixed)	
a ($R_\odot$)	$1.971^{+0.019}_{-0.011}$	
i (°)	$45.20^{+0.13}_{-0.20}$	
T_{eff} (K)	$3894.95.^{+0.69}_{-0.92}$	
q	$0.631^{+0.014}_{-0.003}$	
Spot 1 longitude (°)	$183.80^{+0.28}_{-0.28}$	$315.12^{+0.29}_{-0.66}$
Spot 1 colatitude (°)	$78.83^{+0.80}_{-0.35}$	$65.32^{+0.72}_{-1.85}$
Spot 1 radius (°)	$47.94^{+0.25}_{-0.37}$	$52.04^{+0.51}_{-4.8}$
Spot 1 temp. factor	$0.886^{+0.001}_{-0.003}$	$0.922^{+0.001}_{-0.012}$
Spot 2 longitude (°)	⋯	$157.57^{+0.65}_{-0.43}$
Spot 2 colatitude (°)	⋯	$81.95^{+0.49}_{-1.82}$
Spot 2 radius (°)	⋯	$24.07^{+2.21}_{-0.30}$
Spot 2 temp. factor	⋯	$0.691^{+0.071}_{-0.013}$

3.4. Radio and X-Ray Detection

The FAST searches have failed to identify a radio pulsar signal from J1527. In our 40 minute and 50 minute searches, we can infer a flux density upper limit of 6 μJy and 5 μJy at 1250 MHz, respectively. Here, we assume a minimum detectable signal-to-noise ratio S/N$_{\mathrm{min}} = 10$ and a 20% duty cycle. At the Gaia EDR3 distance, we obtain X-ray luminosities of $(9.30 \pm 3.32) \times 10^{28}$ erg s^{-1} in the 0.1–2.4 keV PSPC range of the RASS. The low X-ray luminosity of the system is consistent with a quiescent dwarf nova or the chromospherically active RS CVn system (Demircan 1987). Therefore, the X-ray emission can originate from one of them or a mixture of both but may also be an NS.
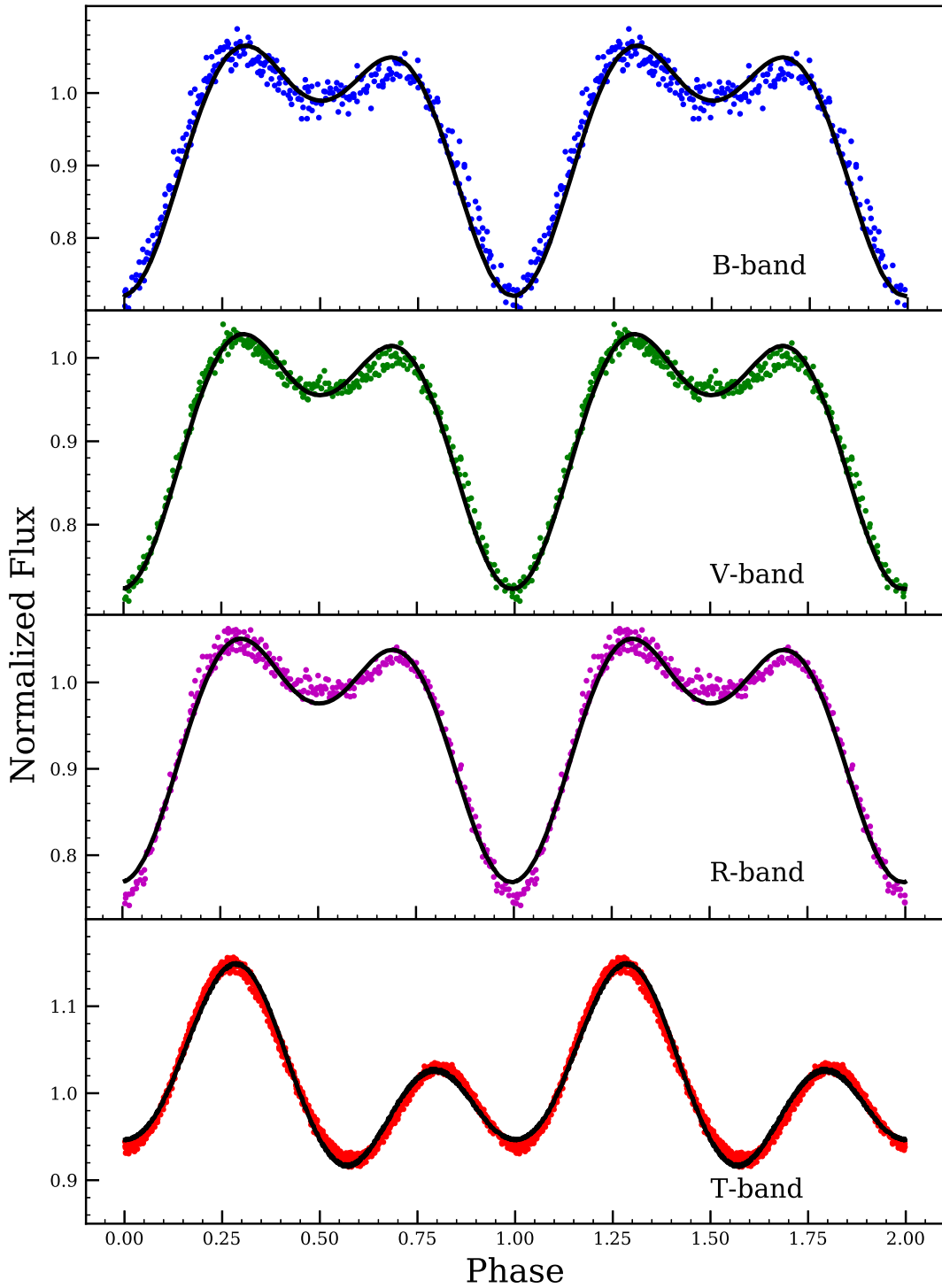
Figure 6. The normalized *B*-, *V*-, *R*-band and TESS light curves for J1527 as a function of orbital phase. The black solid line represents the best-fitting model from PHOEBE.

4. Discussion

4.1. Is the Compact Companion in J1527 a White Dwarf?

The mass of the compact object ($M_c = 0.98 \pm 0.03\,M_\odot$) in J1527 may suggest it can be a white dwarf in a cataclysmic variable (CV) (an interacting binary system with a white dwarf companion). However, we lay out the arguments that the compact companion in J1527 as a white dwarf will suffer some trouble. It is found that the narrow component of H_α is in antiphase with the radial-velocity curve of the visible star,

which may give an indication of the possible presence of an accretion disk. The result helps us immediately rule out that the source belongs to the polar class. This is because polars have a strong magnetic field in the range of $\sim$10–300 MG, preventing the formation of an accretion disk (Cropper 1990). For a polar-type CV, it is worth noting that a broad H_α component may also originate in an accretion stream between the two stars (Schwope et al. 2020). However, the narrow component originates from the unseen companion in J1527, while the broad component is in phase with the absorption-line radial

velocity. If the narrow component is due to an accretion stream rather than an accretion disk, the compact star may be a polar. In intermediate polars (IPs), the magnetic field is somewhat smaller and a partial accretion disk is usually present, and the white dwarf does not corotate with the orbit (Patterson 1994). Here, the source has a very low X-ray luminosity, which is not consistent with any known X-ray luminosity of IPs. In addition, the observed low X-ray luminosity is also consistent with low-accretion-rate polars (LARPS) when a white dwarf accretes at an extremely low rate from the wind of the visible donor star (Schwope et al. 2009). Therefore, the source as a candidate for a polar or an IP looks problematic if the narrow H_α component indeed is from an accretion disk. However, it is not possible to assess whether it is a polar or an IP using the present data.

A final discussion concerns dwarf novae, a class of nonmagnetic CVs in which the system undergoes outbursts to brighten by several magnitudes lasting from days to weeks. The outbursts are thought to be caused by disk instabilities when the accretion disk reaches a critical density. J1527 has been detected by the deep GALEX far- and near-ultraviolet (FUV and NUV), and the measured flux of the NUV is about five times higher than that of the FUV, which indicates an ultraviolet excess from the K9-M0-type star. In fact, the observed Ca II H&K and H_α emission are present in the low-resolution spectra of J1527 as common indicators of chromospheric activities, which seemingly suggest that the deep GALEX FUV and NUV result from stellar chromospheric activity. However, the luminosity of the FUV ($4.07 \pm 0.57 \times 10^{29}$ erg s^{-1}) and NUV ($2.10 \pm 0.09 \times 10^{30}$ erg s^{-1}) is an order of magnitude higher than the chromospheric luminosity, which is not consistent with the chromospheric activities of a late-type star (Stelzer et al. 2016). However, we do not exclude the chromospheric contribution from the late-type star. In order to subtract the UV contribution from chromospheric activity, we estimate the chromospheric contribution at FUV and NUV. The median EW of the H_α emission is ~ 2.72. We can convert the H_α at the surface using $F_\alpha = \mathrm{EW}(\alpha) F_c$ (Soderblom et al. 1993), where F_c is the continuum flux at H_α that we drive using the flux calibration of Hall (1996), $\log F_c = 7.538 - 1.08 (B - V)_0$. We obtain $(B - V)_0 = 1.28 \pm 0.01$ mag using the APASS DR10 photometry. Then, using the empirical relation ($\log L_{\mathrm{NUV}} / L_{\mathrm{bol}} = 0.67 \log(L_\alpha / L_{\mathrm{bol}}) - 0.85$) of Jones & West (2016), we can obtain the NUV of $\sim 1.24 \times 10^{-16}$ erg s^{-1} cm^{-2} Å^{-1}. For FUV, we obtain $R'_{\mathrm{HK}} = 4.1$ using the $\log R'_{\mathrm{HK}}$–$\log P_{\mathrm{rot}}$ relationship of Astudillo-Defru et al. (2017). According to the relation ($\log R'_{\mathrm{FUV}} = (0.98 \pm 0.05) \log R'_{\mathrm{HK}} + (-0.53 \pm 0.25)$) of Findeisen et al. (2011), the FUV flux can be calculated as $\sim 1.46 \times 10^{-17}$ erg s^{-1} cm^{-2} Å^{-1}. Here, we subtract the visible-star flux and the chromospheric contribution at FUV and NUV.

Therefore, the FUV and NUV excess may stem from either a white dwarf or an accretion disk. If we assume that the FUV excess of J1527 is from the white dwarf, its effective temperature T_{eff} is about 12,000 K by adopting a mass of $M_{\mathrm{WD}} = 1.0 M_\odot$ and a radius of $R \sim 5 \times 10^8$ cm (Figure 7). Then, we can utilize $T_{\mathrm{eff}} = 12,000$ K to estimate the accretion rates $\dot{M}$ using the equation of Townsley & Gänsicke (2009):

$$T_{\mathrm{eff}} = 17,000 (\langle \dot{M} [M_\odot \, \mathrm{yr}^{-1}] \rangle / 10^{-10})^{1/4}$$
$$(M_{\mathrm{wd}} [M_\odot] / 0.9) \, \mathrm{K}. \quad (3)$$

Using the estimated temperature of the white dwarf derived from the FUV emission, we can obtain accretion rates of

$\dot{M} \sim 1.63 \times 10^{-11} M_\odot$ yr^{-1}. The inferred value of the mass-transfer rate is far below the critical accretion rate that would be needed to keep the thermal-viscous disk in a stable state at this orbital period (Dubus et al. 2018), which suggests that J1527 should exhibit dwarf nova phenomena. However, there is no evidence for the dwarf nova outburst in our long time-series archives data (see Figure 1). We also note that the fraction of dwarf novae above the period gap can remain in quiescence due to the low accretion rates or large accretion disk (Sokolovsky et al. 2022). If we consider that approximately half of the gravitational energy of the accreting gas is liberated through X-rays in the boundary layer, then for an $M_c \sim 1.00 M_\odot$ white dwarf, the inferred accretion rate of $\dot{M} \sim 1.63 \times 10^{-11} M_\odot$ yr^{-1} implies the X-ray luminosity of $\sim 1.38 \times 10^{32}$ erg s^{-1}. If assume that the observed X-ray luminosity originates entirely from the released gravitational energy of the accreting gas, it is a factor of ~ 1000 below the inferred X-ray luminosity. However, if a white dwarf has a lower temperature in J1527, it will also mean a lower accretion rate or X-ray luminosity. In summary, we cannot completely rule out that the compact object is a white dwarf in J1527.

4.2. Is the Compact Companion an "X-Ray-dim Isolated Neutron Star" in Binary J1527?

Then, we consider a scenario where the compact companion is a low-mass NS. If the compact companion is not a white dwarf in J1527, then it is a low-mass X-ray binary (LMXB) containing either an NS or BH companion. However, the mass of the compact companion immediately rules out a stellar BH, which means the most likely scenario is an NS. We did not detect the radio pulsations from J1527 in two observations using FAST, which may suffer from severe scattering and/or absorption due to the system being enshrouded by intrabinary material. In addition, the lack of the detection of radio pulsations in two observations may result from eclipses due to the ephemeris probably not being accurate enough. If so, there should be a γ-ray counterpart due to the interaction between the pulsar wind and the accretion disk. However, we did not find a possible γ-ray counterpart to J1527 from the Fermi-LAT catalog. Therefore, we propose that the dark companion of J1527 is likely an XDINS-like compact object in binary.

The most direct interpretation to account for a low X-ray luminosity is that none or parts of the accretion flow reach the NS surface when the magnetospheric radius r_{m} is much larger than the corotation radius r_{co} according to standard accretion theory (Illarionov & Sunyaev 1975). Here, we interpret that the FUV and NUV come from an accretion disk (Takata et al. 2014), which is consistent with the presence of a narrow H_α emission. We use one blackbody to fit the FUV and NUV with the Python package lmfit.[13] The modeled temperature is $T = 12,500^{+500}_{-690}$ K with the corresponding radius $R = 5.23^{+0.82}_{-0.48} \times 10^8$ cm. Here, we make the simplified assumption that the corresponding radii R_{BB} is consistent with the magnetospheric radius r_{m}. The magnetospheric radius is

$$r_{\mathrm{m}} = 1.2 \times 10^9 \mu_{29}^{4/7} \dot{M}_{13}^{-2/7} \left(\frac{M}{M_\odot} \right)^{-1/7} \sim 5.23 \times 10^8 \, \mathrm{cm}, \quad (4)$$
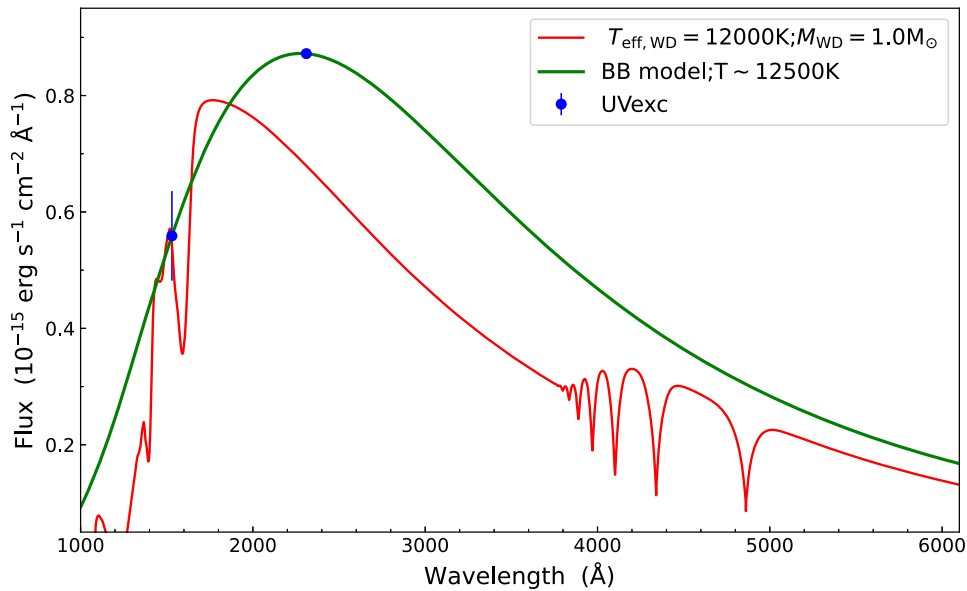
---
[13] https://lmfit.github.io/lmfit-py/

Figure 7. The green line is a blackbody model, while the red line is a DA-type white dwarf of $1.0M_\odot$ with $T_{\mathrm{eff,WD}} = 12{,}000\mathrm{K}$.

where the magnetic moment $\mu = B_{\mathrm{p}}R^3/2 \sim 10^{29}B_{\mathrm{p,11}}$ G cm^3 and the radius of the NS is $R = 12$ km. The observed $L_{\mathrm{bol}} = GM\dot{M}/2r_{\mathrm{m}} \sim 4.78 \times 10^{30}$ erg s^{-1}, derived from the one-blackbody model, which gives the disk accretion rate $\dot{M} = 3.74 \times 10^{13}$ g s^{-1}. According to Equation (4) and the disk accretion rate, we obtain a weak magnetic field of $\sim B_{\mathrm{P}} = 4.53 \times 10^{10}$ G for an NS. The system is in the propeller regime when the magnetospheric radius is larger than the corotation radius ($r_{\mathrm{m}} > r_{\mathrm{c}}$). In this picture, the NS with a weak magnetic field must have a spin period $P_{\mathrm{spin}} < 6.50$ s since the corotation radius is

$$r_c = (GMP^2/4\pi^2)^{1/3} = 1.50 \times 10^8 P^{2/3} \text{ cm.} \qquad (5)$$

Considering a radio-quiet NS with a weak magnetic field, it may be located at the radio pulsar death line because the electric potential of the gap region is too low to generate electron–positron pairs. This also accounts for the absence of γ rays in the system. Using the radio pulsar death line $B_{\mathrm{p}}/P^2 = 1.7 \times 10^{11}$ G s^{-2} (Bhattacharya et al. 1992), we obtain the spin period of the death line $P_{\mathrm{spin}} \sim 0.52$ s. Therefore, we estimate the spin period of the NS $0.52 \text{ s} \leqslant P_{\mathrm{spin}} \leqslant 6.50$ s, which is also consistent with the characteristic spin period of the XDINS (Kaplan et al. 2011). In addition, the hardness ratio from the RASS uncovers a relatively soft emission. This may suggest that the X-ray emission is from an NS although the soft X-ray emission also appears to be consistent with a chromospheric origin.

In addition, a dynamically discovered NS with $M_{\mathrm{c}} \sim 1.00$ $M_\odot$ will be the lightest NS, which challenges the paradigm of gravitational-collapse NS formation (Lattimer 2012). However, a low-mass limit (0.9–1.1 $M_\odot$) is also suggested when considering that both thermal and neutrino-trapping effects are large (Goussard et al. 1998; Strobel et al. 1999). If supernova explosions cannot possibly produce an NS with a mass smaller than about $1.17M_\odot$ (Suwa et al. 2018), the

compact object of J1527 may be a strange star. Recently, the analysis of the central compact object (CCO) within the supernova remnant HESS J1731–347 reported an NS with $M = 0.77^{+0.20}_{-0.17}M_\odot$ based on modeling of the X-ray spectrum and a robust distance (Doroshenko et al. 2022). In addition, Doroshenko et al. (2016) present evidence that the CCO of the supernova remnant HESS J1731–347 could have been formed within a binary system. Based on some similarities between the NSs of both HESS J1731–347 and J1527, this may imply that they may be born via the same channel. More interestingly, the discovery that the radionuclide ^{60}Fe signal observed in deep-sea crusts is global indicates multiple supernova events during the last 10 million years within $\sim$100 pc of Earth (Wallner et al. 2016; Ertel et al. 2022; Zheng et al. 2022). The XDINS-like compact object at a distance of $\sim$118 pc makes it the nearest NS, which may suggest the radionuclide ^{60}Fe signal from deep-sea crusts is associated with its supernova event. Furthermore, we performed a kinematic analysis of J1527's orbit in the galaxy using the Gaia astrometric solution and the systematic radial velocity (see Appendix B), and it implies that it can pass through our solar neighborhood and is consistent with residing in the Galactic thin disk.

The discovery of a compact object in J1527 likely implies that some XDINS-like objects remain in a binary when they receive low kicks at birth. As a result, there may be lots of XDINS-like stars, either as a single or in binaries, in the Milky Way since these NSs are dim and close to us. Our findings may hint at XDINS-like compact objects possibly being born in an alternative channel rather than in standard core-collapse supernovae, as discussed for the accretion-induced collapse (AIC) of an ONeMg white dwarf (Taani 2022), for instance.

5. Conclusions

We identify a K9-M0-type star with chromospheric activity in a binary system with a dark companion mass of $M_{\mathrm{c}} = 0.98 \pm 0.03$ $M_\odot$. By modeling the multiband light curve

with PHOEBE, we derive an inclination of $45°20^{+0°13}_{-0°20}$, a mass ratio of $0.631^{+0.014}_{-0.003}$, and the K9–M0-type star's mass of $0.62 \pm 0.01\,M_\odot$ using constraints on the radial velocity, orbital period, and stellar temperature. The medium-resolution LAMOST spectrum uncovers H_α emission of a wider range and another peak emission, suggesting the presence of an accretion disk. Here, the dark companion mass of $M_c = 0.98 \pm 0.03\,M_\odot$ is either a white dwarf or an NS. However, the system shows some characteristics that seem to contradict it being a cataclysmic variable, such as the lack of any observed outburst in the 5193 day time series of optical observations. Therefore, we discuss the other possibility that the unseen compact companion is a low-mass NS. If the dark companion is confirmed as an NS, it will be the nearest and lightest NS yet. These features, together with being X-ray dim and radio quiet, are similar to those of XDINSs, and we thus suggest the J1527 binary may host an XDINS-like compact object.

To determine the nature of the compact object and understand this unique system, further multiband observations are necessary. The observation of the Hubble Space Telescope spectroscopy will especially determine whether the compact object is a white dwarf, and X-ray observations may also address the nature of the compact object.

Appendix A
Short Timescale Variability in the Residuals

There is extra variability on the timescales of hours in the residuals of the *B*-, *V*-, and *R*-band and TESS *T*-band light curves after subtracting the best model, which may result from disk oscillations known as superhumps (Zurita et al. 2002; Ramsay et al. 2017). In addition, the residuals exhibit similar characteristics in the light curves (Figure A1). We searched for
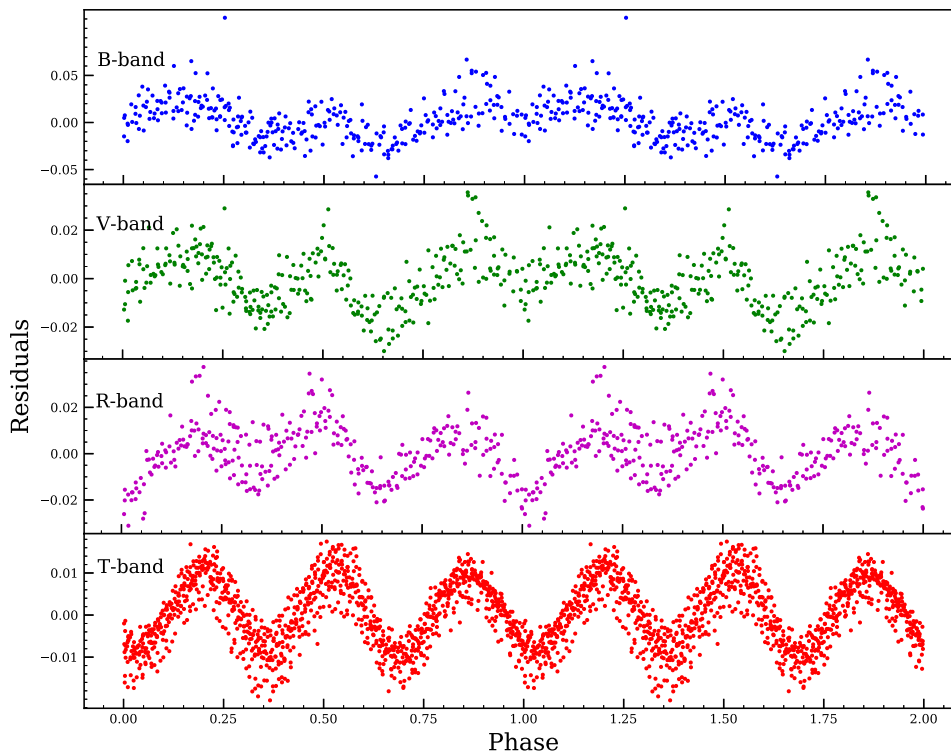

Figure A1. The light-curve residuals for multiple bands (*B, V, R,* and *T*) after the PHOEBE model is subtracted.

additional variability on the timescale of hours in the TESS *T*-band light curve and find no evidence of variability in any other period. Further, there is no periodic signal after prewhitening the data on the main period using higher-cadence observations for the *B*, *V*, and *R* bands. Therefore, the residuals of the light curve show quasi-sinusoidal signals, which might not be induced by disk oscillations (superhumps). Here, we can see clear evidence of structure in the residuals, which may be from stellar pulsation, random noise, and systematic calibration noise (Welsh et al. 2011).

Appendix B
The Kinematic Analysis of J1527

We use the Gala code to compute J1527's trajectory around the Milky Way over 50 Myr (Price-Whelan 2017), using the Milky Way potential. Here, we use the parallax and proper motion reported by Gaia, and the systematic radial velocity fitted by our radial-velocity data (Figure B1). This suggests that J1527 resides in the Galactic thin disk and the system passed through our solar neighborhood in the past.
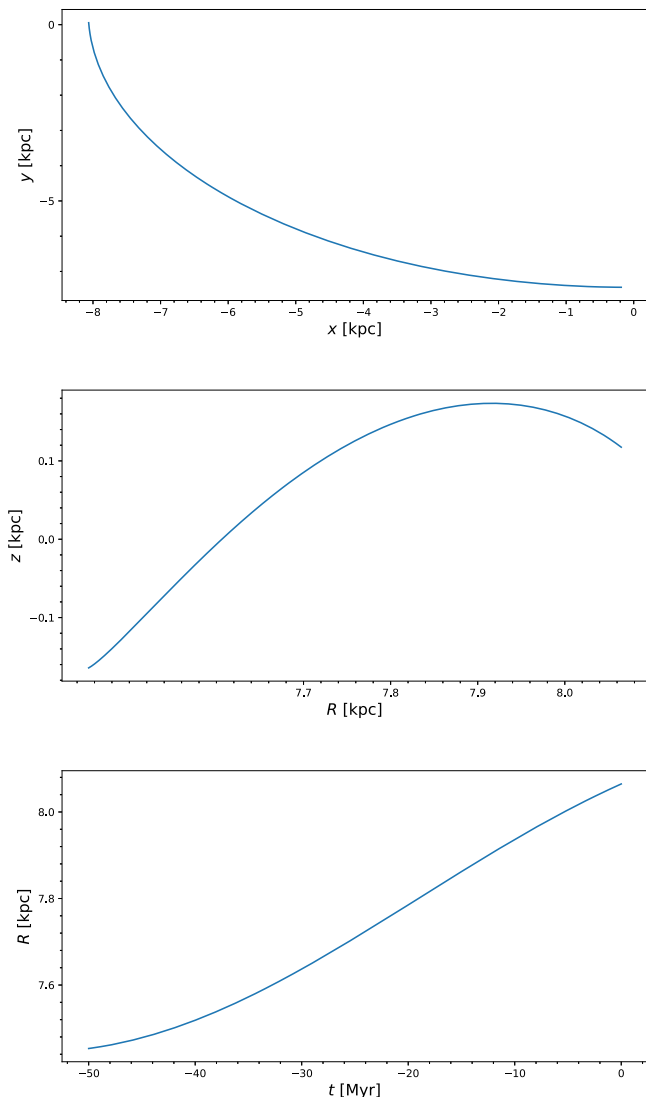

Figure B1. A set of panels showing the trajectory of J1527 around the Milky Way integrated backwards from the present day for 50 Myr.

ORCID iDs

Jie Lin ⓘ https://orcid.org/0000-0001-6311-6391
Chunqian Li ⓘ https://orcid.org/0000-0002-6647-3957
Weiyang Wang ⓘ https://orcid.org/0000-0001-9036-8543
Heng Xu ⓘ https://orcid.org/0000-0002-5031-8098
Jinchen Jiang ⓘ https://orcid.org/0000-0002-6465-0091
Shuguo Ma ⓘ https://orcid.org/0000-0001-5066-5682
Hubiao Niu ⓘ https://orcid.org/0000-0001-5796-8010
Ali Esamdin ⓘ https://orcid.org/0000-0003-1845-4900
Gavin Ramsay ⓘ https://orcid.org/0000-0001-8722-9710
Jianrong Shi ⓘ https://orcid.org/0000-0002-0349-7839
Renxin Xu ⓘ https://orcid.org/0000-0002-9042-3044

References

Astudillo-Defru, N., Delfosse, X., Bonfils, X., et al. 2017, A&A, 600, A13
Boller, T., Freyberg, M. J., Trümper, J., et al. 2016, A&A, 588, A103
Bai, C. H., Feng, G. J., Zhang, X., et al. 2020, RAA, 20, 211
Bertin, E., & Arnouts, S. 1996, A&AS, 117, 393
Butters, O. W., West, R. G., Anderson, D. R., et al. 2010, A&A, 520, L10
Bhattacharya, D., Wijers, R. A. M. J., Hartman, J. W., et al. 1992, A&A, 254, 198
Cropper, M. 1990, SSRv, 54, 195
Casares, J. 2001, Binary Stars: Selected Topics on Observations and Physical Processes, ed. F. C. Lazaro & M. J. Arevalo (Berlin: Springer), 277
Castelli, F., & Kurucz, R. L. 2003, in IAU Symp. 210, Modeling of Stellar Atmospheres (San Francisco, CA: ASP), A20
Conroy, K. E., Kochoska, A., Hey, D., et al. 2020, ApJS, 250, 34
Drake, A. J., Graham, M. J., Djorgovski, S. G., et al. 2014, ApJS, 213, 9
Demircan, O. 1987, Ap&SS, 137, 195
Doroshenko, V., Puhlhofer, G., Kavanagh, P., et al. 2016, MNRAS, 458, 2565
Dubus, G., Otulakowska-Hypka, M., & Lasota, J.-P. 2018, A&A, 617, A26
Doroshenko, V., Suleimanov, V., Pühlhofer, G., et al. 2022, NatAs, 6, 1444
Ertel, A. F., Fry, B. J., Fields, B. D., et al. 2022, arXiv:2206.06464
Foreman-Mackey, D., Farr, W., Sinha, M., et al. 2019, JOSS, 4, 1864
Fryer, C. L., Belczynski, K., Wiktorowicz, G., et al. 2012, ApJ, 749, 91
Findeisen, K., Hillenbrand, L., & Soderblom, D. 2011, AJ, 142, 23
Gaia Collaboration, Brown, A. G. A., Vallenari, A., et al. 2018, A&A, 616, A1
Gaia Collaboration, Brown, A. G. A., Vallenari, A., et al. 2021, A&A, 649, A1
Goussard, J.-O., Haensel, P., & Zdunik, J. L. 1998, A&A, 330, 1005
Green, G. M., Schlafly, E., Zucker, C., et al. 2019, ApJ, 887, 93
Gu, W. M., Mu, H. J., Fu, J. B., et al. 2019, ApJL, 872, L20
Hall, J. C. 1996, PASP, 108, 313
Haberl, F., Motch, C., Zavlin, V. E., et al. 2004, A&A, 424, 635
Haberl, F. 2007, Ap&SS, 308, 181
Hartman, J. D., Bakos, G. Á, Noyes, R. W., et al. 2011, AJ, 141, 166
Ho, W. C. G., Kaplan, D. L., Chang, P., Van Adelsberg, M., & Potekhin, A. Y. 2007, MNRAS, 375, 821
Illarionov, A. F., & Sunyaev, R. A. 1975, A&A, 39, 185
Lattimer, J. M. 2012, ARNPS, 62, 485
Jones, D. O., & West, A. A. 2016, ApJ, 817, 1
Jiang, P., Tang, N. Y., Hou, L. G., et al. 2020, RAA, 20, 064
Jayasinghe, T., Stanek, K. Z., Thompson, T. A., et al. 2021, MNRAS, 504, 2577
Jayasinghe, T., Stanek, K. Z., Kochanek, C. S., et al. 2019, MNRAS, 486, 1907
Kaplan, D. L., Kamble, A., van Kerkwijk, M. H., et al. 2011, ApJ, 736, 117
Kaspi, V. M. 2010, PNAS, 107, 7147
Langer, N. 2012, ARA&A, 50, 107
Liu, J., Zhang, H., Howard, A. W., et al. 2019, Natur, 575, 618
Mukai, K. 2017, PASP, 129, 062001
Mann, A. W., Dupuy, T., Kraus, A. L., et al. 2019, ApJ, 871, 63
Pires, A. M., Motch, C., & Janot-Pacheco, E. 2009, A&A, 504, 185
Pires, A. M., Motch, C., Turolla, R., et al. 2015, A&A, 583, A117
Price-Whelan, A. M., Hogg, D. W., Foreman-Mackey, D., et al. 2017, ApJ, 837, 20
Price-Whelan, A. M. 2017, JOSS, 2, 388
Patterson, J. 1994, PASP, 106, 209
Ransom, S. M. 2001, PhD Thesis, Harvard Univ.
Ramsay, G., Wood, M. A., Cannizzo, J. K., Howell, S. B., & Smale, A. 2017, MNRAS, 469, 950
Rigoselli, M., Mereghetti, S., & Tresoldi, C. 2022, MNRAS, 509, 1217
Soderblom, D. R., Stauffer, J. R., Hudon, J. D., et al. 1993, ApJS, 85, 315
Strobel, K., Schaab, C., & Weigel, M. K. 1999, A&A, 350, 497

Schwope, A. D., Nebot Gomez-Moran, A., Schreiber, M. R., et al. 2009, A&A, 500, 867

Silaj, J., Jones, C. E., Tycner, C., et al. 2010, ApJS, 187, 228

Sokolovsky, K. V., Strader, J., Swihart, S. J., et al. 2022, ApJ, 934, 142

Suwa, Y., Yoshida, T., Shibata, M., Umeda, H., & Takahashi, K. 2018, MNRAS, 481, 3305

Strader, J., Chomiuk, L., Cheung, C. C., et al. 2015, ApJL, 804, L12

Stelzer, B., Damasso, M., Scholz, A., & Matt, S. P. 2016, MNRAS, 463, 1844

Schwope, A. D., Worpel, H., Webb, N. A., et al. 2020, A&A, 637, A35

Tody, D. 1986, Proc. SPIE, 627, 733

Tody, D. 1993, in ASP Conf. Ser. 52, Astronomical Data Analysis Software and Systems II, ed. R. J. Hanisch, R. J. V. Brissenden, & J. Barnes (San Francisco, CA: ASP), 173

Townsley, D. M., & Gänsicke, B. T. 2009, ApJ, 693, 1007

Thompson, T. A., Kochanek, C. S., Stanek, K. Z., et al. 2019, Sci, 366, 637

Takata, J., Li, K. L., Leung, G. C. K., et al. 2014, ApJ, 785, 131

Taani, A. 2022, arXiv:2210.08125

Vines, J. I., & Jenkins, J. S. 2022, MNRAS, 513, 2719

Voges, W., Aschenbach, B., Boller, T., et al. 1996, IAU Circ., 6420, 2

Voges, W., Aschenbach, B., Boller, T., et al. 1999, A&A, 349, 389

Wang, Z., Archibald, A. M., Thorstensen, J. R., et al. 2009, ApJ, 703, 2017

Welsh, W. F., Orosz, J. A., Aerts, C., et al. 2011, ApJS, 197, 4

Wallner, A., Feige, J., Kinoshita, N., et al. 2016, Natur, 532, 69

Wang, W., Lu, J., Tong, H., et al. 2017, ApJ, 837, 81

Wang, W. Y., Feng, Y., Lai, X. Y., et al. 2018, RAA, 18, 082

Woosley, S. E., Sukhbold, T., & Janka, H. T. 2020, ApJ, 896, 56

Yi, T., Gu, W. M., Zhang, Z. X., et al. 2022, NatAs, 6, 1203

Yuan, H., Wang, S., Bai, Z., et al. 2022, ApJ, 940, 165

Zurita, C., Casares, J., Shahbaz, T., et al. 2002, MNRAS, 333, 791

Zhao, G., Zhao, Y. H., Chu, Y. Q., Jing, Y. P., & Deng, L. C. 2012, RAA, 12, 723

Zong, W., Fu, J. N., De Cat, P., et al. 2020, ApJS, 251, 15

Zheng, L. L., Sun, M., Gu, W. M., et al. 2022, arXiv:2210.04685